Multibody Dynamics Versus Fluid Dynamics: Two Perspectives on the Dynamics of Granular Flows

Milad Rakhsha
Department of Mechanical Engineering,
University of Wisconsin-Madison,
Madison, WI 53706
e-mail: rakhsha@wisc.edu

Conlain Kelly
Department of Mechanical Engineering,
University of Wisconsin-Madison,
Madison, WI 53706
e-mail: ckelly5@wisc.edu

Nic Olsen
Department of Mechanical Engineering,
University of Wisconsin-Madison,
Madison, WI 53706
e-mail: nicholas.olsen@wisc.edu

Radu Serban
Department of Mechanical Engineering,
University of Wisconsin-Madison,
Madison, WI 53706
e-mail: serban@wisc.edu

Dan Negrut
Department of Mechanical Engineering,
University of Wisconsin-Madison,
Madison, WI 53706
e-mail: negrut@wisc.edu

Considering that granular material is second only to water in how often it is handled in practical applications, characterizing its dynamics represents a ubiquitous problem. However, studying the motion of granular material poses stiff computational challenges. The underlying question in this contribution is whether a continuum representation of the granular material, established in the framework of the smoothed particle hydrodynamics (SPH) method, can provide a good proxy for the fully resolved granular dynamics solution. To this end, two approaches described herein were implemented to run on graphics processing unit (GPU) cards to solve the three-dimensional (3D) dynamics of the granular material via two solution methods: a discrete one, and a continuum one. The study concentrates on the case when the granular material is packed but shows fluid-like behavior under large strains. On the one hand, we solve the Newton–Euler equations of motion to fully resolve the motion of the granular system. On the other hand, we solve the Navier–Stokes equations to describe the evolution of the granular material when treated as a homogenized continuum. To demonstrate the similarities and differences between the multibody and fluid dynamics, we consider three representative problems: (i) a compressibility test (highlighting a static case); (ii) the classical dam break problem (highlighting high transients); and (iii) the dam break simulation with an obstacle (highlighting impact). These experiments provide insights into conditions under which one can expect similar macroscale behavior from multibody and fluid dynamics systems governed by manifestly different equations of motion and solved by vastly different numerical solution methods. The models and simulation platform used are publicly available and part of an open source code called Chrono. Timing results are reported to gauge the efficiency gains associated with treating the granular material as a continuum.
[DOI: 10.1115/1.4047237]

1 Introduction

From an application standpoint, the class of rigid multibody dynamics problems of interest in this work pertains granular flows. These macroscopic flows are shaped/dictated by microscopic friction and contact interactions. However, fully resolved simulations of granular material dynamics that trace microscopic interactions are computationally expensive. In fact, in many applications the number of elements considered is not dictated by the physics of the actual problem, but rather by constraints on the duration of the simulation. To the best of our knowledge, the largest fully resolved granular dynamics simulation of practical relevance reported in the literature contained 2.4×10^9 elements. Among other hardware platforms, it was run on 16,384 central processing units (CPUs) (131,072 cores) of Japan's K-supercomputer [1–3], the 2012 fastest supercomputer in the world and, at the time of the experiment, the 18th in the ranking of the world's supercomputers [4]. To put the "2.4×10^9 elements" number in perspective, in one cubic meter of sand, depending on the type of sand, there are one to two billion discrete elements. Practical examples of applications in which granular dynamics comes into play include mobility on deformable terrains, landslides, avalanches, food processing, farming, etc. It becomes apparent that the scale of many of these applications calls for systems which have in excess of two billion elements. Given today's state of the art, fully resolved solutions to these problems are likely infeasible. This observation provides the backdrop for this contribution, which seeks to gauge the extent to which the fully resolved representation of the granular material can be replaced with a continuum one that leverages the so-called smoothed particle hydrodynamics (SPH) method [5,6].

The premise of this work is that if only the macroscale characteristics of the system are of interest, in large-scale granular flow problems, a continuum approximation is likely to be more expeditious than the discrete methodology while providing adequate accuracy. To make this point, the contribution discusses and compares two solutions to the granular dynamics problem—a fully resolved one, drawing on classical discrete element method (DEM) [7] and anchored in the Newton–Euler equations of motions; and a continuum one, that draws on fluid dynamics and the incompressible Navier–Stokes equations.

Granular material may behave like solids (a sand pile), liquids (pouring from a silo), or even gases (separation and collision of grains). In this study, the interest is in the first two scenarios. One factor that makes the dynamics of the granular material complex is the strain-rate dependency of the shear stress, a trait also encountered in fluid dynamics. However, unlike in fluids, in granular dynamics there exists a threshold value (yield criterion) under which the grains do not move relative to each other but rather their emergent collective behavior becomes solid-like—elastic and/or plastic. This characteristic, combined with the fluid-like feature of the media, might suggest for granular material a viscoplastic constitutive law, similar to the one used in non-Newtonian fluids [8]. However, the behavior of granular material is richer than what a viscoplastic model would capture [9]. Among various models and theories developed previously, the $\mu(I)$-rheology [10] for granular material homogenization is one of the more successful frameworks matching observations from a variety of experimental and numerical results. More recent approaches rely on hybrid solutions, wherein a representative volume element is treated in a fully resolved fashion, with the information harvested at the microscale subsequently embedded into a continuum representation of the overall flow [11–14].

Contributed by the Design Engineering Division of ASME for publication in the Journal of Computational and Nonlinear Dynamics. Manuscript received December 15, 2019; final manuscript received May 12, 2020; published online July 16, 2020. Assoc. Editor: Massimo Ruzzene.

The flow of granular materials is governed by the Newton–Euler equations of motion, whereas the Navier–Stokes equations capture the momentum balance in fluids. Pressure and viscous forces arise in fluids from the normal and shear stresses, respectively, but these quantities are not tied together for Newtonian fluids. In granular media, frictional forces depend on the normal forces through Coulomb's friction model; stated differently, shear stresses correlate with normal stresses. Informed by this observation, a constitutive law for granular media is proposed in Ref. [10] using the incompressible fluid model with a suitably chosen *effective viscosity*. This effective viscosity factors in the value of the friction coefficient and it is also tied to the pressure, the latter being a proxy for normal stress in granular materials. Hence, this rheology relates the shear stress to the normal stress, which is indeed the expected behavior in granular media. More recent efforts focused on overcoming shortcomings of the local constitutive model were outlined in Ref. [10] by incorporating nonlocal effects for nonuniform slow flows [9,15].

This paper is concerned with the case in which the friction forces in a granular medium and the viscous stresses in a fluid medium are insignificant compared to the normal forces in the granular medium and pressure in the fluid medium, respectively. The highlights of the contribution are as follows: (i) it includes three studies that demonstrate that a fully three-dimensional (3D) continuum implementation using SPH can serve as a good proxy for granular dynamics; in this context, it also compares run times that confirm that starting with relatively small discrete problems the continuum implementation discussed is more attractive than a fully resolved one; and (ii) the results presented are obtained with an open-source, publicly available tool called Chrono [16,17] that has support for both representations—discrete or continuum. The contribution is organized as follows. In Sec. 2, we describe the equations governing the physics of the fluid and solid phases, along with the numerical techniques employed to approximate their solution (motion). Specifically, in Secs. 2.1 and 2.1.1 we, respectively, describe the Navier–Stokes equations and the SPH method as the space-discretization technique for the numerical solution. The DEM in the context of the Newton–Euler equations is described in Sec. 2.2.1. In Sec. 3, we present the numerical results of the experiments performed using the multibody and the fluid dynamics solvers. A discussion of the similarities and differences noted in the dynamics of the two media is presented in Sec. 4. Concluding remarks and future directions of research are provided in Sec. 5.

2 Governing Equations and Numerical Methods

2.1 Continuum Model. The Lagrangian forms of the mass conservation and Cauchy momentum balance for a continuum assume the expression [18]

$$\frac{D\rho}{Dt} - \rho\nabla\cdot\boldsymbol{u} = 0 \tag{1}$$

$$\frac{D(\rho\boldsymbol{u})}{Dt} - \nabla\cdot\boldsymbol{\sigma} - \boldsymbol{f}_b = 0 \tag{2}$$

where $\boldsymbol{u}$ is the velocity, ρ is the density, and $\boldsymbol{f}_b$ represents the distributed body force. Conventionally, $\boldsymbol{\sigma}$ is decomposed into a volumetric (hydrostatic) part and a deviatoric part, $\boldsymbol{\sigma} = \boldsymbol{\sigma}^{\text{dev}} + \boldsymbol{\sigma}^{\text{vol}}$, where with $p \equiv -(\sigma_{11}+\sigma_{22}+\sigma_{33})/3$ denoting the mechanical pressure we have $\boldsymbol{\sigma}^{\text{vol}} \equiv p\boldsymbol{I}_{3\times3}$. This allows for an equivalent reformulation of the momentum balance

$$\frac{D(\rho\boldsymbol{u})}{Dt} + \nabla p - \nabla\bullet\boldsymbol{\sigma}^{\text{dev}} - \boldsymbol{f}_b = \boldsymbol{0} \tag{3}$$

For Newtonian fluids, the deviatoric part of the stress tensor is related to the shear rate, through $\boldsymbol{\sigma}^{\text{dev}} = 2\mu\boldsymbol{E}$, where μ is a constant representing the dynamic viscosity of the fluid and the strain-rate tensor $\boldsymbol{E}$ is obtained from the velocity gradient tensor as

$$\boldsymbol{E} = \frac{1}{2}(\nabla\mathbf{u} + \nabla\mathbf{u}^T) \tag{4}$$

Given that $\nabla\cdot\boldsymbol{u} = 0$ for incompressible flows, Eq. (3) is simplified under incompressible flow and a Newtonian fluid model to

$$\frac{D(\rho\boldsymbol{u})}{Dt} + \nabla p - \mu\nabla^2\boldsymbol{u} - \boldsymbol{f}_b = \boldsymbol{0}$$

The adimensionalized equations may be written as [19]

$$\frac{d\mathbf{u}}{dt} = -\text{Eu}\frac{\nabla p}{\rho} + \frac{1}{\text{Re}}\nabla^2\mathbf{u} + \frac{1}{\text{Fr}^2}\mathbf{f}^b \tag{5}$$

where the Euler number, $\text{Eu} = (p_0/\rho_0 u_0^2)$, is the ratio of the pressure to inertia forces (or static pressure to dynamic pressure). The Reynolds number, $\text{Re} = (\rho u_0 L_0/\mu)$, may be seen as the ratio of inertia to viscous forces. Finally, the Froude number, $\text{Fr} = (U_0/\sqrt{g_0 L_0})$, may be regarded as the ratio of inertia to body forces. For inviscid fluids, $\mu = 0$, and the $(1/\text{Re})\nabla^2\mathbf{u}$ term drops out of the equations, in which case the momentum balance is the interplay of inertia, pressure, and gravity/body force. In other words, the equations come down to the conservative Euler equations, for which the relative significance of different terms is characterized by the magnitude of the Fr and Eu numbers.

While the viscosity in Newtonian fluids is constant, in non-Newtonian fluid models it depends on several parameters, e.g., yield stress, shear-rate, etc. In this context, several models have been proposed to capture shear thinning, shear-thickening, and yield stress. The one employed in this work is the Herschel–Bulkley model. Defining the shear stress and shear strain-rate from their underlying tensors according to, respectively,

$$\tau = \sqrt{2\boldsymbol{\sigma}_{ij}^{\text{dev}} : \boldsymbol{\sigma}_{ij}^{\text{dev}}}$$
$$\dot{\gamma} = \sqrt{2\boldsymbol{E}_{ij} : \boldsymbol{E}_{ij}}$$

the Herschel–Bulkley model describes the stress–strain-rate relation via

$$\tau = \tau_0 + k\dot{\gamma}^n \tag{6}$$

where $k > 0$ is a consistency index, and n is the flow index. The Herschel–Bulkley model captures various fluid behaviors using a combination of n and k, as illustrated in Fig. 1. This includes shear thickening (dilatant), shear thinning (pseudo-plastic), and Bingham plastic models. Subsequently, an apparent (effective) space-dependent viscosity satisfying $\tau = \mu_{\text{eff}}\dot{\gamma}$ and Eq. (6) may be defined as [21]

$$\mu_{\text{eff}} = \tau_0/\dot{\gamma} + k\dot{\gamma}^{n-1} \tag{7}$$

Finally, the deviatoric stress in the momentum balance is written as $\boldsymbol{\sigma}^{\text{dev}} = 2\mu_{\text{eff}}\boldsymbol{E}$, where $\boldsymbol{E}$ is defined in Eq. (4). This definition of $\boldsymbol{\sigma}^{\text{dev}}$ keeps with the one for Newtonian fluids with the caveat that one has to replace the constant μ with a state dependent μ_{eff}.

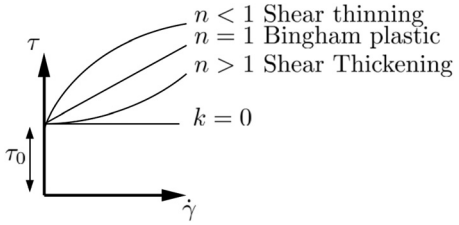

Fig. 1 Stress–strain-rate relationship for different flow index and consistency parameters in Herschel–Bulkley model [20]

Given the incompressible flow assumption, the $\nabla \cdot \boldsymbol{\sigma}^{\text{dev}}$ term in Eq. (3) is written as

$$\begin{aligned}\nabla \cdot \boldsymbol{\sigma}^{\text{dev}} &= \nabla \cdot (\mu_{\text{eff}}(\nabla \mathbf{u} + \nabla \mathbf{u}^T)) \\ &= \mu_{\text{eff}} \nabla \cdot (\nabla \boldsymbol{u}) + \nabla \mu_{\text{eff}} \cdot \nabla \boldsymbol{u} + \mu_{\text{eff}} \nabla (\nabla \cdot \boldsymbol{u}) + \nabla \mu_{\text{eff}} \cdot \nabla \boldsymbol{u}^T \\ &= \mu_{\text{eff}} \nabla^2 \boldsymbol{u} + \nabla \mu_{\text{eff}} \cdot (\nabla \boldsymbol{u} + \nabla \boldsymbol{u}^T) \end{aligned} \tag{8}$$

The final form of the momentum balance for non-Newtonian fluids in a Lagrangian framework is [22]

$$\frac{D(\rho \boldsymbol{u})}{Dt} + \nabla p - \mu \nabla^2 \boldsymbol{u} - \nabla \mu_{\text{eff}} \cdot (\nabla \boldsymbol{u} + \nabla \boldsymbol{u}^T) - \boldsymbol{f}_b = 0 \tag{9}$$

As the intent is to establish a fluid model that represents a proxy for granular dynamics, since the latter is dominated at the microscale by Coulomb friction that ties the normal and tangential loads via $F_t \leq \mu_g F_N$, it is helpful to tie the non-Newtonian's model yield stress (see Eq. (6)) to pressure via $\tau_0 = \mu_g p$, where μ_g is the local friction coefficient in granular material [10]. Here, the subscript g is used to distinguish the friction coefficient in granular medium, μ_g, from the fluid viscosity μ. Accordingly, the effective granular viscosity in Eq. (7) for $k = 0$ may be written as

$$\mu_{\text{eff}} = \frac{\mu_g p}{\dot{\gamma}} \tag{10}$$

A robust and accurate numerical implementation of the yield stress in the Navier–Stokes equations is still a matter of research [20]. The difficulty lies in modeling the discontinuity arising from the yield stress, as the material should only flow if the shear stress exceeds the yield stress τ_0 (see Fig. 1). In other words

$$\begin{cases} \text{yielded region:} & \tau > \tau_0 \\ \text{unyielded region:} & \tau < \tau_0 \end{cases} \tag{11}$$

This discontinuity cannot be strictly enforced for truly unyielded regions in a continuum if one chooses to use a non-Newtonian approach since this approach does not have an elastic component that keeps the material together prior to yielding. An alternative is to solve the time-evolution of the stress tensor side-by-side with the Navier–Stokes and continuity equations, using a rate of shear stress defined as [23,24]

$$\frac{d\sigma^{\alpha\beta}}{dt} = 2G\left(E^{\alpha\beta} - \frac{1}{3}\delta^{\alpha\beta}E^{\gamma\gamma}\right) - \sigma^{\alpha\gamma}\omega^{\gamma\beta} + \omega^{\alpha\gamma}\sigma^{\gamma\beta}$$

where G is the shear modulus, and $\boldsymbol{\omega}$ is the rotation tensor

$$\boldsymbol{\omega} = \frac{1}{2}(\nabla \mathbf{u} - \nabla \mathbf{u}^T)$$

The approach involves the scaling of the stress tensor back to the yield surface once the stress grows beyond the yield criteria. The results for this approach will be reported elsewhere. Herein, the focus will be on gauging how well the continuum representation can serve as a proxy for the dynamics of the granular material in frictionless regime ($\mu_g = 0$).

2.1.1 Spatial Discretization of the Continuum. For the continuum representation, the SPH method is employed for the spatial discretization of Eqs. (1) and (2). The SPH approximation for a scalar field assumes the form [25]

$$f(\mathbf{r}_i) \approx \langle f \rangle_i = \sum_{j \in \mathcal{S}(i)} \frac{m_j}{\rho_j} f(\mathbf{r}_j) W_{ij}$$

where $\langle f \rangle_i$ indicates the SPH approximation of f at the location of SPH marker i; $\mathcal{S}(i)$ represents the collection of SPH markers found in the support domain associated with marker i; ρ_j is the density $\rho(\mathbf{r}_j)$ at location $\mathbf{r}_j$ of marker j; $m_j = \rho_j V_j$ and $V_j = \left(\sum_{k \in \mathcal{S}(j)} W_{jk}\right)^{-1}$ are the mass and volume associated with marker j, respectively; and $W_{ij} \equiv W(\mathbf{r}_i - \mathbf{r}_j, h)$, with W a suitable chosen kernel function. The cubic spline kernel for 3D problems adopted herein is expressed as

$$W(q,h) = \frac{5}{14\pi h^3} \times \begin{cases} (2-q)^3 - 4(1-q)^3, & 0 \leq q < 1 \\ (2-q)^3, & 1 \leq q < 2 \\ 0, & q \geq 2 \end{cases} \tag{12}$$

where $q \equiv |\mathbf{r}_{ij}|/h$. The radius of the support domain, κh, is proportional to the characteristic length h through the parameter κ, the latter commonly set to 2 for the cubic spline kernel as shown in Fig. 2.

The standard SPH approximation of the gradient and Laplacian of the function f assumes the following form [25]

$$\nabla f(\mathbf{r}_i) = \langle \nabla f \rangle_i = \sum_{j \in \mathcal{S}(i)} V_j \nabla_i W_{ij} (f_j - f_i)$$

$$\nabla^2 f(\mathbf{r}_i) = \langle \nabla^2 f \rangle_i = 2 \sum_{j \in \mathcal{S}(i)} V_j (\mathbf{e}_{ij} \cdot \nabla_i W_{ij}) \frac{f_i - f_j}{|\mathbf{r}_{ij}|}$$

where $\mathbf{e}_{ij} \equiv \mathbf{r}_{ij}/|\mathbf{r}_{ij}|$. The expression for the gradient of the kernel function described in Eq. (12) is

$$\begin{aligned}\nabla_i W_{ij} &= \frac{\mathbf{r}_{ij}}{|\mathbf{r}_{ij}|} \frac{\partial W}{\partial q} \frac{\partial q}{\partial |\mathbf{r}_{ij}|}\bigg|_{i,j} \\ &= \frac{-15\mathbf{r}_{ij}}{14\pi h^5 q} \times \begin{cases} (2-q)^2 - 4(1-q)^2, & 0 \leq q < 1 \\ (2-q)^2, & 1 \leq q < 2 \\ 0, & q \geq 2 \end{cases} \end{aligned} \tag{13}$$

In Eq. (13), ∇_i denotes the differentiation in space with respect to the coordinates of SPH marker i.

2.1.2 Time Integration. We apply an implicit SPH (ISPH) method which uses the Helmholtz–Hodge decomposition and Chorin's projection method [26] to integrate the continuity and the Navier–Stokes equation as

$$\text{prediction} \begin{cases} \dfrac{(\mathbf{u}^* - \mathbf{u}^n)}{\Delta t} = \dfrac{\nu}{2}(\nabla^2 \mathbf{u}^* + \nabla^2 \mathbf{u}^n) + \mathbf{f}^b & x \in \Omega \\ \mathbf{u}^* = 0 & x \in \partial\Omega \end{cases} \tag{14}$$

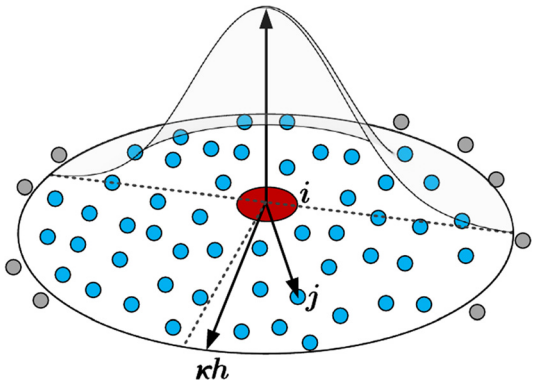

Fig. 2 Two-dimensional illustration of the kernel *W*. The radius of the support domain is defined as a multiple, κ, of the kernel's characteristic length, *h*.

$$\text{correction}\begin{cases}\dfrac{(\mathbf{u}^{n+1}-\mathbf{u}^{*})}{\Delta t}=-\dfrac{1}{\rho}\nabla p^{n+1} & x\in\Omega\\ \nabla.\mathbf{u}^{n+1}=0\end{cases}\tag{15}$$

Equation (14) is the predictor step and it can be used to find the intermediate velocity $\mathbf{u}^{*}$. Taking divergence of Eq. (15), the Poisson equation for pressure is obtained as

$$\frac{\nabla\cdot\mathbf{u}^{n+1}-\nabla\cdot\mathbf{u}^{*}}{\Delta t}=-\frac{1}{\rho}\nabla^{2}p^{n+1}\tag{16}$$

Note that from the mass conservation (Eq. (1)) and the incompressible flow assumption ($(d\rho/dt)=0$), one can write $\nabla\cdot\mathbf{u}^{n+1}=0$ and simplify Eq. (16) to

$$\begin{cases}\dfrac{1}{\rho}\nabla^{2}p^{n+1}=\dfrac{\nabla\cdot\mathbf{u}^{*}}{\Delta t}\\ \nabla p^{n+1}\cdot\mathbf{n}|_{\partial\Omega}=0\end{cases}\tag{17}$$

Next, using the semidiscrete continuity equation

$$\frac{\rho^{*}-\rho^{n}}{\Delta t}=-\rho^{n}\nabla\cdot\mathbf{u}^{*}\tag{18}$$

one may write Eq. (17) as

$$\begin{cases}\dfrac{1}{\rho}\nabla^{2}p^{n+1}=-\dfrac{1}{\rho^{n}}\dfrac{\rho^{*}-\rho^{n}}{\Delta t^{2}}\\ \nabla p^{n+1}\cdot\mathbf{n}|_{\partial\Omega}=0\end{cases}\tag{19}$$

which takes into consideration the density variation as a source term in the Poisson equation. Finally, once the pressure distribution is computed, Eq. (15) may be used to find $\mathbf{u}^{n+1}$ as follows:

$$\mathbf{u}^{n+1}=-\Delta t\frac{1}{\rho}\nabla p^{n+1}+\mathbf{u}^{*}\tag{20}$$

As far as the time-step Δt is concerned, its size is constrained on numerical stability grounds by the following condition [27]

$$\Delta t\le\min\left\{0.25\frac{h}{k|\mathbf{v}|_{\max}},0.125\frac{h^{2}}{\nu},0.25\sqrt{\frac{h}{|\mathbf{f}_{b}|}}\right\}\tag{21}$$

Above, the first term corresponds to the Courant–Friedrichs–Lewy (CFL) condition. The second restriction in Eq. (21) appears due to the explicit treatment of the viscous term and restricts the time-step by a factor that is inversely proportional to the viscosity—the higher the viscosity, the lower the time-step. More importantly, the second restriction is also proportional to h^{2}, which significantly and adversely impacts the time-step when a finer SPH marker distribution is employed. The last restriction is due to the explicit treatment of the external (body) forces.

There are two important observations pertaining to the ISPH method implemented: (a) the Crank–Nicolson discretization of the viscous term in Eq. (14) leads to a nondiagonal coefficient matrix Eq. (14) in its discrete form. Had one chosen to treat the viscous term in Eq. (14) explicitly, that is $\nu\nabla^{2}\mathbf{u}^{n}$ instead of $\frac{\nu}{2}(\nabla^{2}\mathbf{u}^{*}+\nabla^{2}\mathbf{u}^{n})$, the coefficient matrix of the linear system in Eq. (14) would have become a diagonal matrix, $\frac{1}{\Delta t}\mathbf{I}$. Yet this choice that makes the linear solve trivial, would constrain the time-step Δt owing to the explicit treatment of the viscous term, which imposes the time-step restriction $\Delta t<0.125\frac{h^{2}}{\nu}$, see Eq. (21); and, (b) a modification that proved particularly useful at small Δt pertains a scaling of the pressure by a factor Δt^{2} in the Poisson equation, and by $1/\Delta t^{2}$ in the correction step Eq. (15). In other words, we compute $p\Delta t^{2}$ when solving the Poisson equation and subsequently scale the pressure in the correction step Eq. (15) by a factor of $1/\Delta t^{2}$.

Finally, the pressure and viscous forces acting on a boundary marker a, which are required for fluid-structure coupling, can be obtained from the momentum balance equations via

$$\mathbf{F}_{a}=m_{a}\frac{d\mathbf{u}_{a}}{dt}=m_{a}\left(\nu\nabla^{2}\mathbf{u}_{a}^{n+1}-\frac{1}{\rho}\nabla p_{a}^{n+1}\right)\tag{22}$$

2.1.3 Boundary Conditions. In imposing boundary conditions (BCs), we make use of so-called *boundary conditions enforcing* (BCE) markers. These are fictitious markers, rigidly attached to the boundary in a buffer zone that runs several layers deep as shown in Fig. 3. These markers are used to enforce the no-slip and the no-penetration conditions on the boundary.

In one widely used approach [28], the *expected* kinematic attributes of the markers, calculated from the motion of the solid phase at the location occupied by the markers, are different from their *assigned* values. The latter are calculated such that the no-slip and no-penetration boundary conditions are implicitly enforced at the fluid–solid interface. The no-slip condition states that the velocity of the BCE markers should oppose the velocity of the fluid markers such that the average *relative* fluid–solid velocity at the interface is zero. In other words, the average velocity at the interface is the expected interface velocity. Herein, the *induced* velocity $\tilde{\mathbf{u}}_{a}$ at the position of marker a is computed from the velocity of the fluid markers as

$$\tilde{\mathbf{u}}_{a}=\frac{\sum_{b\in\mathbf{F}}\mathbf{u}_{b}W_{ab}}{\sum_{b\in\mathbf{F}}W_{ab}}\tag{23}$$

where $\mathbf{F}$ denotes a set of fluid markers that are within the compact support of the BCE marker a. The no-slip condition holds if $(\tilde{\mathbf{u}}_{a}+\mathbf{u}_{a})/2=\mathbf{u}_{a}^{p}$; in other words, the assigned velocity of marker a is [28]

$$\mathbf{u}_{a}=2\mathbf{u}_{a}^{p}-\tilde{\mathbf{u}}_{a}\tag{24}$$

where $\mathbf{u}_{a}^{p}$ is the expected wall velocity at the position of the marker a, and $\tilde{\mathbf{u}}_{a}$ is an extrapolation of the smoothed velocity field of the fluid phase to the BCE markers.

The pressure of a BCE marker may be calculated via a force balance condition at the wall interface, which leads to [28]

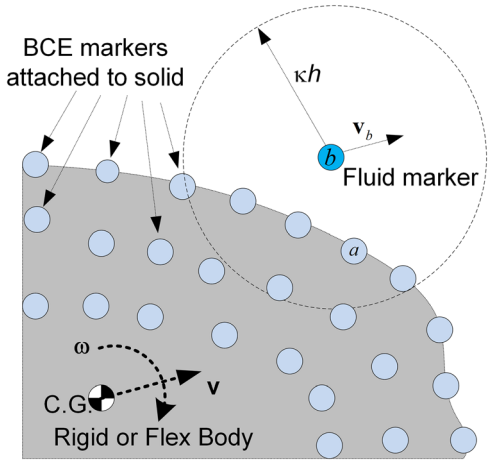

Fig. 3 The BCE markers, which are placed both on the solid's surface and in a thin buffer region inside it, are used toward two ends: transfer surface forces from the fluid subsystem to the solid subsystem and enforce no-slip boundary conditions

$$p_a = \frac{\sum_{b\in\mathbf{F}} p_b W_{ab} + (\mathbf{g} - \mathbf{a}_a^p)\cdot \sum_{b\in\mathbf{F}} \rho_b \mathbf{r}_{ab} W_{ab}}{\sum_{b\in\mathbf{F}} W_{ab}} \tag{25}$$

where $\mathbf{g}$ is the gravitational acceleration and $\mathbf{a}_a^p$ is the acceleration of the boundary/solid at the location of BCE marker a.

2.2 Discrete Model

2.2.1 Rigid Multibody Dynamics With Friction and Contact. The equations of motion for the discrete problem are formulated in the context of the classical discrete element methodology [7]. For element i, let $\mathcal{C}(i;t)$ be the collection of bodies that i is in mutual contact with at time t. The time evolution of sphere i is governed by the momentum balance laws

$$m_i \frac{d\mathbf{v}_i}{dt} = m_i \mathbf{g} + \sum_{j\in\mathcal{C}(i;t)} \left(\mathbf{F}_n^{ij} + \mathbf{F}_t^{ij}\right) \tag{26a}$$

$$I_i \frac{d\boldsymbol{\omega}_i}{dt} = \sum_{j\in\mathcal{C}(i;t)} \mathbf{M}^{ij} = \sum_{j\in\mathcal{C}(i;t)} \Delta\mathbf{r}^{ij} \times \mathbf{F}_t^{ij} + \mathbf{M}_{rr}^{ij} \tag{26b}$$

where for element i, m_i is its mass; I_i is its mass moment of inertia; the velocity $\mathbf{v}_i = \dot{\mathbf{r}}_i$ is the time derivative of the position; $\Delta\mathbf{r}^{ij}$ is the vector from the center of mass to the point where the friction force $\mathbf{F}_t^{ij}$ is applied; and $\mathbf{M}_{rr}^{ij}$ is the rolling resistance moment. Given that all elements are spheres, there is no need to store their orientation and the angular velocity $\boldsymbol{\omega}_i$ will provide the information needed to track the friction history at the point of contact. The normal and tangential forces are determined using the Hertzian and Mindlin contact formulations, respectively,

$$\mathbf{F}_n^{ij} = \sqrt{\frac{\delta^{ij}}{2\overline{R}^{ij}}}\left(k_n \delta^{ij} \mathbf{n}^{ij} - \gamma_n \overline{m}^{ij} \mathbf{v}_n^{ij}\right) + \mathbf{F}_c \tag{26c}$$

$$\mathbf{F}_t^{ij} = \sqrt{\frac{\delta^{ij}}{2\overline{R}^{ij}}}\left(-k_t \mathbf{u}_t^{ij} - \gamma_t \overline{m}^{ij} \mathbf{v}_t^{ij}\right) \tag{26d}$$

Above, $\mathbf{F}_c$ is a cohesion force, $\overline{m}^{ij}$ and $\overline{R}^{ij}$ represent the effective mass and effective radius for the contact, and $\mathbf{v}_n$ and $\mathbf{v}_t$ are the normal and tangential velocities

$$\overline{m}^{ij} = \frac{m_i m_j}{m_i + m_j} \tag{26e}$$

$$\overline{R}^{ij} = \frac{R_i R_j}{R_i + R_j} \tag{26f}$$

$$\mathbf{v}^{ij} = \mathbf{v}_j + \boldsymbol{\omega}_j \times \mathbf{r}_j - \mathbf{v}_i - \boldsymbol{\omega}_i \times \boldsymbol{r}_i \tag{26g}$$

$$\mathbf{v}_n^{ij} = (\mathbf{v}^{ij}\cdot\mathbf{n}^{ij})\mathbf{n}^{ij} \tag{26h}$$

$$\mathbf{v}_t^{ij} = \mathbf{v}^{ij} - \mathbf{v}_n^{ij} \tag{26i}$$

The friction force is capped relative to the normal contact force via the Coulomb condition $|\mathbf{F}_t^{ij}| \le \mu\,|\mathbf{F}_n^{ij}|$.

In order to compute the forces in Eqs. (26*c*) and (26*d*), one must evaluate the contact normal $\mathbf{n}_{ij}$, normal penetration δ^{ij}, tangential displacement at the contact point $\mathbf{u}_t^{ij}$, and normal and tangential components of the relative velocity $\mathbf{v}_n^{ij}$ and $\mathbf{v}_t^{ij}$, respectively. Except for $\mathbf{u}_t^{ij}$ these quantities can be readily computed from the sphere positions, linear velocities, and angular velocities.

The computation of $\mathbf{u}_t^{ij}$ is slightly more involved. Dropping the ij superscripts for notational brevity, $\mathbf{u}_t$ is updated in a multistep fashion, from integration step to integration step, tracking its history between steps. At time-step k, $\mathbf{u}_{t,k}$ stores the tangential displacement history. This quantity is always enforced to be perpendicular to the current contact normal and thus lie in the contact plane

$$\begin{aligned}\mathbf{u}_{t,k}^* &= \mathbf{u}_{t,k-1} + \mathbf{v}_{t,k}\Delta t\\ \mathbf{u}_{t,k} &= \mathbf{u}_{t,k}^* - (\mathbf{n}_k\cdot\mathbf{u}_{t,k}^*)\mathbf{n}_k\end{aligned} \tag{27}$$

The Coulomb capping of the friction force is then enforced via

$$\mathbf{u}_t = \min\left(\mathbf{u}_{t,k}, \mathbf{u}_{t,k}\frac{\mu_s k_n \delta_n}{k_t|\mathbf{u}_{t,k}|}\right) \tag{28}$$

where μ_s is taken to be the same between static and dynamic motions. Note that since the $\sqrt{\frac{\delta^{ij}}{2\overline{R}^{ij}}}$ term appears in both $\mathbf{F}_t$ and $\mathbf{F}_n$, it cancels out of the Coulomb criterion and does not affect clamping. Only the frictional force computed in Eq. (26*d*) is clamped—the rolling resistance torque described below is not affected by the Coulomb criterion.

The quantity $\mathbf{v}_t$ is interpreted as the relative velocity at the contact point including both sliding and rolling contributions. This enforces a situation of "rolling without slipping," where only the relative displacement of the contact point is relevant and not the means of locomotion. An additional rolling resistance torque $\mathbf{M}_{rr}^{ij}$ of Eq. (26*b*) is introduced based on ideas outlined in Refs. [29–32] to bring in an interelement rolling resistance meant to emulate effects induced by roughness and interlocking. Two rolling resistance models are implemented based on work reported in Ref. [31]. The simpler scales a constant torque by the magnitude of the normal component of the contact force

$$|\mathbf{M}_{rr}^{ij}| = \frac{\boldsymbol{\omega}^{ij}}{|\boldsymbol{\omega}^{ij}|}\mu_r \overline{R}|\mathbf{F}_n^{ij}| \tag{29}$$

where $\boldsymbol{\omega}^{ij} = \boldsymbol{\omega}_i - \boldsymbol{\omega}_j$. The second model applies a resistive moment based on the relative slip at the contact point due to relative roll

$$|\mathbf{M}_{rr}^{ij}| = -\mu_r \overline{R}|\mathbf{F}_n^{ij}|(\boldsymbol{\omega}_i r_i - \boldsymbol{\omega}_j r_j) \tag{30}$$

In both cases, the torque is applied at the contact point in the plane perpendicular to $\boldsymbol{\omega}^{ij}$. Table 1 summarizes the parameters associated with the DEM model adopted herein.

Once all contact forces and resultant accelerations are computed for time-step k, the latter are numerically integrated to yield the new velocity and position at time-step $k+1$. Different choices of time-integration methods [33] such as Explicit Euler, Extended Taylor, and a second-order integrator proposed by Chung and Lee [34] are possible. The latter integrator assumes the form

Table 1 Model and simulation parameters

Parameter	Value
N_b	Element count
m	Element mass
g	Gravitational acceleration
R	Element radius
ρ	Element density
k_n	DEM normal elastic coefficient
γ_n	DEM normal damping coefficient
k_t	DEM tangential elastic coefficient
γ_t	DEM tangential damping coefficient
μ_s	Coefficient of static friction
μ_r	Coefficient of rolling friction

Table 2 Bucket simulation: number of discrete elements used for each depth of the granular material

h-value (m)	1.950	1.460	0.979	0.491
N_e (10 mm)	131,218	97,748	64,284	30,761
T_{tot} (10 mm)	71	64	48	30
N_e (5 mm)	1,038,586	767,530	502,461	237,514
T_{tot} (5 mm)	510	390	258	133

Simulation run times for two different particle radii (5 mm and 10 mm) for one second of simulation. Note: T_{tot}—run times (s); N_e—number of elements in the simulation. Relative errors between the continuum and discrete scenarios reported in Fig. 4.

$$\begin{aligned}\mathbf{v}_{k+1} &= \mathbf{v}_k + \Delta t\left(\frac{3}{2}\mathbf{a}_k - \frac{1}{2}\mathbf{a}_{k-1}\right)\\ \mathbf{x}_{k+1} &= \mathbf{x}_k + \mathbf{v}_k\Delta t + (\Delta t)^2\left(\beta\mathbf{a}_k + \left(\frac{1}{2}-\beta\right)\mathbf{a}_{k-1}\right)\end{aligned} \tag{31}$$

It draws on a multistep approach, providing second-order integration for both position and velocity and strong numerical damping. On the down side, the Chung approach requires the caching of previous accelerations $\mathbf{a}_{k-1}$, increasing the memory overhead. It also provides β as a tunable parameter for the integrator's numerical damping, with the stability requirement that $1 \leq \beta \leq \frac{28}{27}$.

2.3 Software Implementation. The fluid and multibody dynamics solutions discussed in Secs. 2.1, 2.1.1, and 2.2.1 have been implemented in an open-source multiphysics simulation platform called Chrono [16] that is freely available online [17,35]. The discrete solver and its implementation are discussed at length in Ref. [36]. Therein, the DEM solver, called Chrono::Granular, was capable of handling problems with more than one billion degrees-of-freedom. A detailed description of the SPH-based fluid dynamics solver in Chrono as well as validation and verification of the solver is provided in Refs. [37] and [38]. Both the fluid and multibody dynamics solvers are parallelized to run on NVIDIA GPUs (Santa Clara, CA), which expose an architecture and programming model suitable for fine-grained parallelism of the single-instruction-multiple-data type encountered in SPH and DEM.

3 Numerical Experiments

3.1 Incompressibility Test. In this benchmark test, we consider a static regime: a bucket filled up with granular material in one case, and with fluid at rest in the second case. The cross section of the bucket is a square of side L. We compare the magnitude of the average force on the side walls of the container for both media. This averaged force changes vertically. For the continuum, there exists an analytical solution that comes from basic fluid hydrostatics. Indeed, the pressure distribution is linear across the depth of the bucket—the larger the depth, the higher the force impressed on the wall. Consequently, it is easy to show that the *averaged* pressure (normal) force on each side of the container is $\rho g h^2 L/2$, where h is the depth of the fluid in the square bucket. Furthermore, the ratio of this force to the weight of the material in the bucket for a $L \times L \times h$ fluid domain is $r_f = h/2L$. DEM simulations were performed to evaluate this ratio for granular media. We calculate this ratio in granular material according to $r_g = \frac{\overline{|\mathbf{F}_n|}}{Mg}$, where $\overline{|\mathbf{F}_n|}$ is the averaged normal forces across the side walls of the container, M is the total mass of the system, and g is the gravity. Densities for both the continuum and granular material are $\rho = 1000\,\text{kg/m}^3$. Finally, we calculate the relative error according to $e = (r_f - r_g/r_f) \times 100$. As shown in Fig. 4, the relative error for $L = 1$ m is small and decreasing with the value of h. This is not unexpected, given that at large element counts, the granular material is better approximated by a continuum.

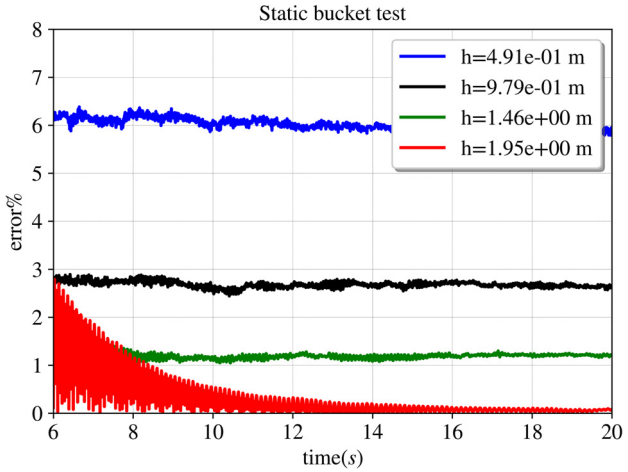

Fig. 4 The relative error of dimensionless normal force experienced by the side walls of a bucket of material for different height (h) of material. The relative error is calculated according to $e = (r_f - r_g/r_f) \times 100$, where r_f is the nondimensional averaged fluid normal force and r_g is the nondimensional averaged granular normal force on the side walls. The r_g is calculated from the DEM simulation while r_f is computed from hydrostatic fluids. A particle radius of 1 cm was used for discrete simulations. Timing results for the discrete element simulation provided in Table 2.

We hypothesize that there should be very good agreement between the two media for this test and attribute the relative error seen in Fig. 4 to mainly two factors: (i) when h is small, the "homogenization" assumption is not holding well for shallow bulk material made up of elements with relatively large radii; and (ii) numerical errors associated with approximating the height of the granular material bucket from the elements' information. It is important to note that the DEM simulations were performed with *frictionless monodisperse spherical* elements. We emphasize that r_g is different in the presence of friction. A detailed discussion on the interplay between friction forces and side walls, as well as on the sensitivity of the results with respect to the elements' shape goes beyond the scope of this contribution and is the subject of ongoing work.

3.2 Dam Break. The "dam break" is a classical fluid mechanics experiment aimed at validating the accuracy and stability

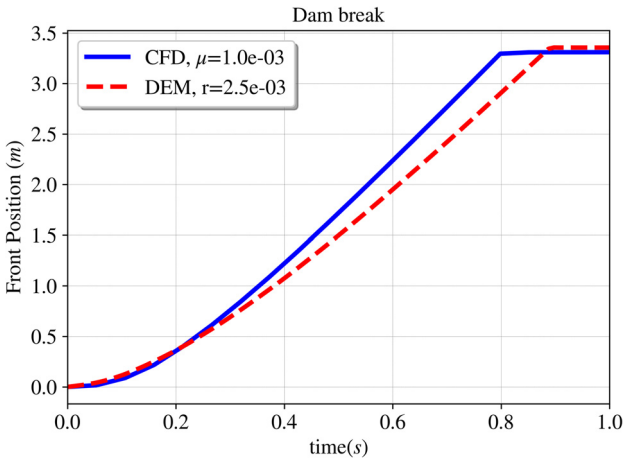

Fig. 5 Comparison of the front position in the dam break simulated with DEM and CFD. DEM experiments simulated 148,438 and 18,939,589 particles for the particle radii 2.5 cm and 0.5 cm, respectively.

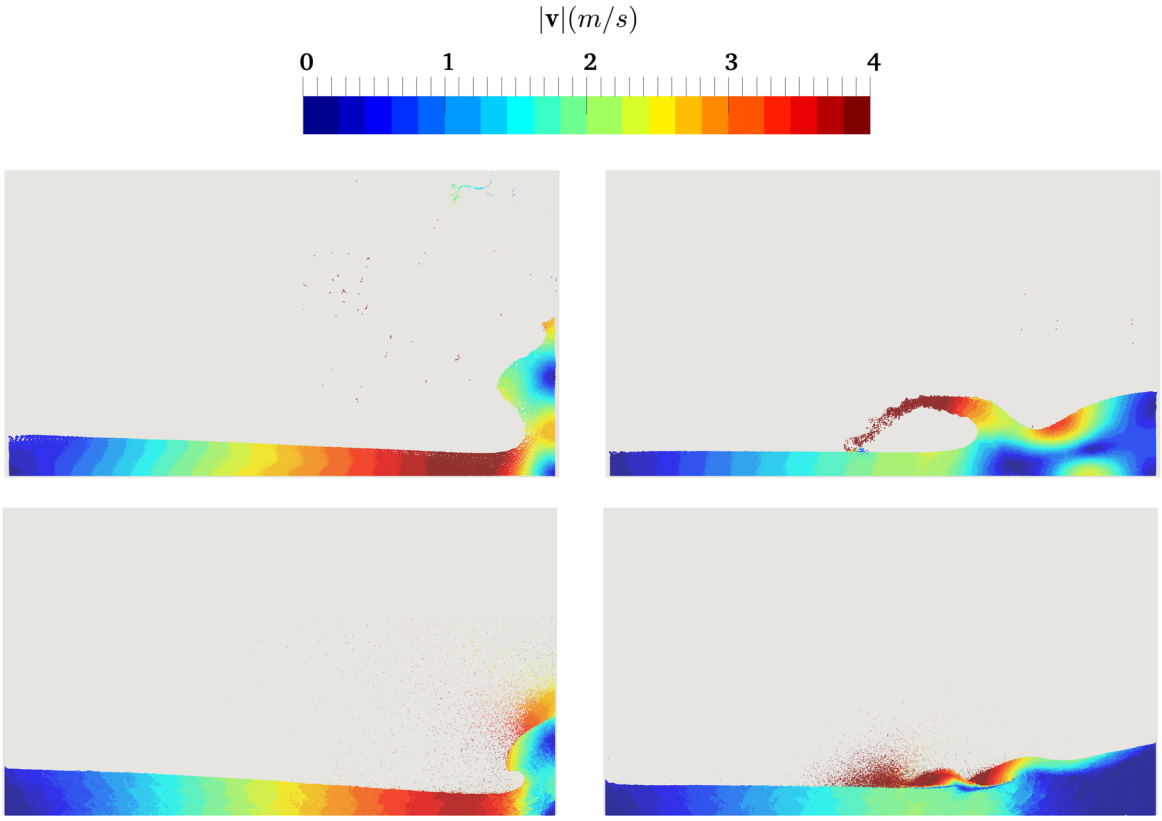

Fig. 6 Comparison of the roll up (left) and the second splash (right) instances of the dam break simulation between granular (bottom) and fluid (top) mediums

characteristics of multiphase solvers. Succinctly, material is stored in a box that is instantaneously removed to allow the flow of the material (fluid or granular) inside. The box containing the material is $2\,\text{m} \times 4\ \text{m} \times 2\ \text{m}$; the dimensions of the container in which the material flows are $6\,\text{m} \times 4\ \text{m} \times 4\ \text{m}$. The reference density is $\rho = 1000\,\text{kg/m}^3$, and the gravity of $g = -9.8\,\text{m/s}^2$ is applied in the y direction.

We study the propagating wave front both in granular material flow and the fluid flow. We highlight the similarities in terms of front speed as shown in Fig. 5, and the differences in terms of two characteristics of the dam break simulation: the *roll up* and the *second splash* [38], see Fig. 6. On the computational fluid dynamics (CFD) side, a more ample discussion of this test may be found in Refs. [28] and [38].

Considering that the CFD and DEM solvers drew on different governing equations, the similarity seen in terms of front propagation position is remarkable. However, as shown in Fig. 5, the front predicted by the DEM simulation moves slightly slower than the one predicted by the CFD solver. We attribute this discrepancy to the bulk density of the material; applying $\rho = 1000\,\text{kg/m}^3$ to individual grains results in smaller overall density in granular material. This is true because of the nature of the packing in granular material, which allows for empty spaces between the grains. This feature, for example, guarantees that a bucket of sand is lighter that a bucket of fluid, assuming that the density of grains is equal to density of the fluid and the buckets have similar dimensions. Hence, we hypothesize that the slower front speed is due to the presence of the voids/empty pockets in the granular material.

3.3 Dam Break With an Obstacle. The setup for this experiment is identical to the one in Sec. 3.2. However, we place a rigid cylindrical obstacle in front of the dam and monitor the overall force experienced by the cylinder over time after the dam breaks. The dam is placed in the leftmost corner of the domain and a 4 m

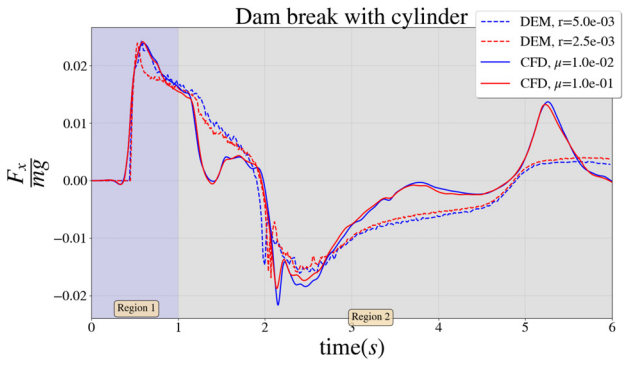

Fig. 7 Comparison of the normalized horizontal force experienced by the cylinder in the dam break simulation for different viscosities of the fluid and for different marker diameters of the granular media

tall cylinder with the radius of 0.3 m is placed at $x = 5$ m from the leftmost side of the container. Figure 7 demonstrates the force experienced by the cylinder for both the granular and fluid materials for different fluid's viscosities, and different grain diameters. As shown in Fig. 7, within the simulated range, the viscous forces in the fluid simulation do not play a major role in the overall force on the cylinder. For granular flow, the force exerted on the cylinder is virtually insensitive to the elements' diameter. The DEM simulation used spheres of radii 2.5 cm and 0.5 cm for a total of 148,438 and 18,939,589 elements, respectively.

Assuming insignificant viscous contribution due to the larger Reynolds number observed in this problem, the fluid flow represents a momentum balance between the *inertia*, *gravity*, and *pressure* forces (see Eq. (5)). As highlighted in Fig. 7, we can consider two different stages in the simulation. *Region 1*: in this stage,

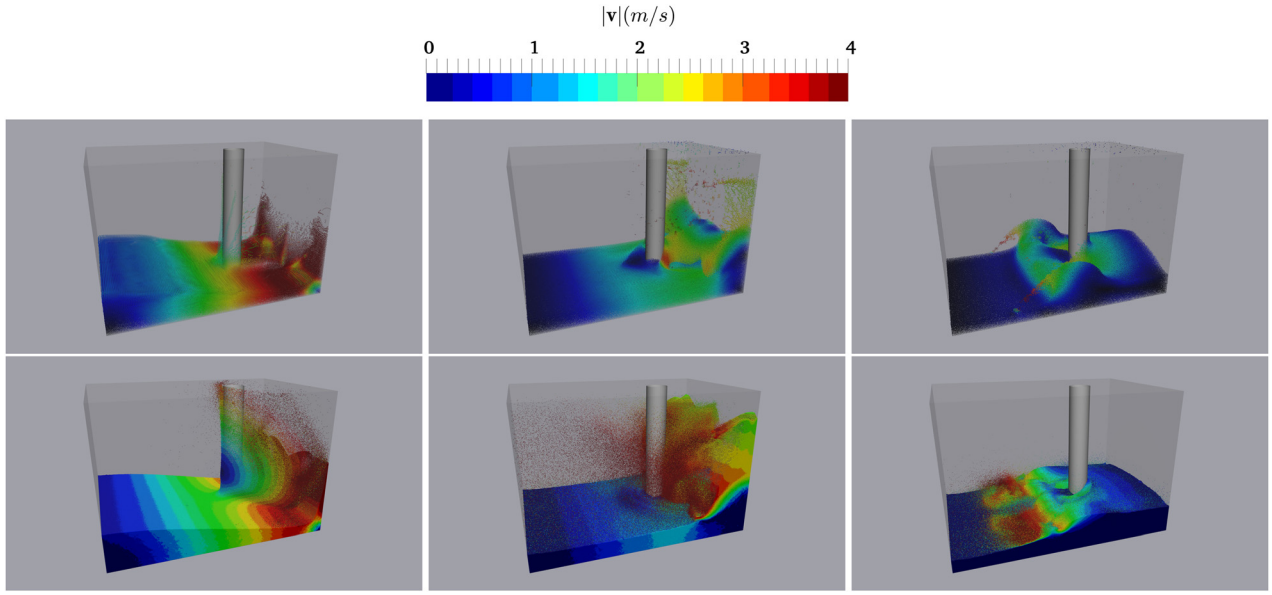

Fig. 8 Snapshots of the fluid (top) and the granular material (bottom) simulation of the dam break with a cylindrical obstacle at $t = 1$ s (left), $t = 2$ s (middle), $t = 2.75$ s (right)

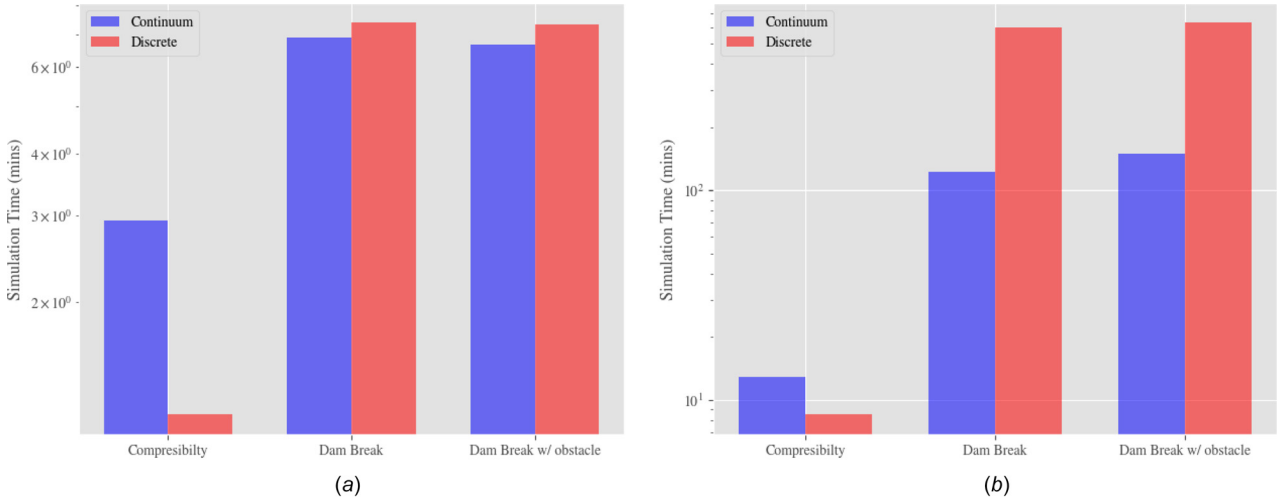

Fig. 9 Comparison of the simulation time—continuum versus discrete, for the resolutions discussed in Table 3: (*a*) low resolution and (*b*) high resolution

good agreement is observed between the two media. We hypothesize that this is true because of the dominant effects of inertia forces over pressure forces. Due to larger values of the velocity, the Euler number ($\mathrm{Eu} = (p_0/\rho_0 u_0^2)$) is relatively small, diminishing the contribution of the normal stress (pressure). *Region 2*: the agreement between the two media is gradually diminishing owing to the different nature of normal forces in granular media compared to pressure gradient forces in fluid flow. This is due to the reduction of the inertia forces and the consequent augmentation of the pressure forces, as can be understood from the Eu number. In Fig. 8, snapshots of the fluid and granular flow simulations are shown for a qualitative comparison of the time evolution of the two media.

4 Discussion

The three experiments considered in this study suggest that in certain regimes, the discrete and continuum models show similar *macroscale* response. We hypothesize that $\mathrm{Eu} = (p_0/\rho_0 u_0^2)$ is the important characteristic number when identifying the regimes in which the granular flow may behave similar to the fluid flow.

According to Eq. (5), as $\mathrm{Eu} \to \infty$, the momentum balance becomes an interplay between the pressure and body forces in fluids. Similarly, the sum of normal contact forces balances the body force in granular media (see Eq. (26*a*)). Hence, it is reasonable to assume that in this regime the pressure plays a role similar to the normal force acting on an element in the granular system. Consequently, in this regime, a continuum model of granular material should be able to predict a potential field whose gradient corresponds to the sum of normal forces. The experiment in which we considered a static bucket of material is an example of flow in this regime where due to $u_0 \to 0$, one has that $\mathrm{Eu} \to \infty$ and $\mathrm{Fr} \to 0$.

At the other end of the spectrum, as $\mathrm{Eu} \to 0$, the contribution of the pressure forces decreases in fluids and the momentum balance is dominated by inertia forces and gravity/body force effects. Similarly, looser packings reduce the contribution of the normal forces in granular material, making the momentum balance an interplay between the inertia and body forces. Hence, we

Table 3 The number of markers and elements in the continuum and discrete models, respectively, for two resolutions

Simulation	C–LR	D–LR	C–HR	D–HR
Compressibility (bucket test)	10k	131k	101k	1,038k
Dam break	63k	148k	303k	18,939k
Dam break with obstacle	64k	148k	312k	18,939k

Note: D—discrete; C—continuum; LR—low resolution; HR—high resolution; and "k" after a number indicates thousands ($\times 10^3$).

hypothesize that the granular material behaves like a fluid in this regime as well.

In terms of computational costs, the SPH fluid solver inherently involves more expensive computations *per* degree-of-freedom. This is primarily due to the fact that each fluid's marker, through the SPH interpolation scheme, interacts with considerably more markers than the granular material element does through mutual contact with other elements. Specifically, one SPH marker might interact with 100 other markers, while an element in the granular material interacts on average with four or five other elements. Furthermore, the fluid solver uses a semi-implicit integration method whereas the granular material solver uses a fully explicit method. Subsequently, (i) higher step sizes are achieved via the fluid solver, yet (ii) each integration step of the fluid solver is more expensive as it requires the solution of a linear system. Figure 9 illustrates the computational time of the continuum and discrete model for the experiment discussed before. The details about the resolution of the solvers for the experiment discussed previously are presented in Table 3.

The results in Fig. 9 confirm that the computational cost of the continuum solver is higher than or comparable with that of the discrete solver for similar degree-of-freedom counts (see Fig. 9(*a*)). However, the continuum approximation allows for the handling of discrete systems with large number of bodies using substantially fewer degrees-of-freedom, see the two "–HR" columns in Table 3. Thus, if one is interested, for instance, in submillimeter granular materials or clays, a fully resolved discrete representation is infeasible and the continuum approach becomes the only viable alternative.

5 Conclusion

This contribution focused on a quantitative comparison between the dynamics of granular material, when approached as a multibody dynamics problem, and the flow of fluids. We compared the motion of a fluid with the flow of granular media made up of *monodisperse spherical frictionless* elements. To that end, two numerical solutions were implemented—the first drawing on the Newton–Euler equations of multibody dynamics, the second on the Navier–Stokes equations for incompressible fluids. We discussed two flow regimes, corresponding to Eu $\rightarrow 0$ and Eu $\rightarrow \infty$, in which similarities are observed in the response of the two media. The Eu $\rightarrow \infty$ case is associated with a scenario in which the sum of normal forces on grains is a conservative force field that mirrors a similar potential field, that is, the fluid pressure.

Two topics stand to be investigated in the future. First, it remains to assess to what extent viscosity can be a proxy for the friction force in granular material. Such an investigation would benefit from the fact that the solver used here supports friction in the DEM and viscosity in the SPH solutions. Second, we plan to further investigate and draw a parallel between the fluid's pressure gradient forces on the one hand and the granular contact normal forces on the other hand. The ultimate goal is that of replacing the time-consuming solution of the fully resolved, multibody dynamics problem, with the solution of a continuum problem that works with an appropriately defined viscosity model. An additional hurdle will be posed by scenarios in which the granular material is not made of identical elements. In this context, there are two relevant and difficult questions that require further investigation: what happens if the spherical granular material is polydisperse? and, can flows of granular material of nontrivial shapes (ellipsoids, for instance) be modeled using the continuum approaches discussed here? We anticipate that the answers to these questions will be consequential in any large body-count problems when the particle size is very small and contact stiffness is large. Under these conditions, the computational burden for fully resolved system is prohibitive and the feasible solutions to the granular dynamics problem will be anchored by continuous formulations.

Funding Data

- National Science Foundation (Grant No. CMMI-1635004 (first author); Funder ID: 10.13039/100000001).
- DURIP instrumentation Army Research Office (Grant No. W911NF1810476; Funder ID: 10.13039/100000183).
- Army Research Office (Grant No. W911NF1910431; Funder ID: 10.13039/100000183).

References

[1] Furuichi, M., Nishiura, D., Asai, M., and Hori, T., 2017, "Poster: The First Real-Scale DEM Simulation of a Sandbox Experiment Using 2.4 Billion Particles," Supercomputing Conference, Denver, CO, Nov., Poster No. 21.

[2] Furuichi, M., Nishiura, D., Kuwano, O., Bauville, A., Hori, T., and Sakaguchi, H., 2018, "Arcuate Stress State in Accretionary Prisms From Real-Scale Numerical Sandbox Experiments," Nat. Sci. Rep., **8**(1), p. 12.

[3] Nishiura, D., Sakaguchi, H., and Yamamoto, S., 2018, "Multibillion Particle DEM to Simulate Centrifuge Model Tests of Geomaterials," *Physical Modelling in Geotechnics* (Proceedings of the 9th International Conference on Physical Modelling in Geotechnics (ICPMG 2018)), Vol. 1, CRC Press, London, p. 227.

[4] Strohmaier, E., Dongarra, J., Simon, H., and Meuer, M., 1997, "TOP500 Supercomputer Sites," Supercomputer, **13**, pp. 89–111.

[5] Lucy, L. B., 1977, "A Numerical Approach to the Testing of the Fission Hypothesis," Astron. J., **82**, pp. 1013–1024.

[6] Gingold, R. A., and Monaghan, J. J., 1977, "Smoothed Particle Hydrodynamics-Theory and Application to Non-Spherical Stars," Mon. Not. R. Astron. Soc., **181**(3), pp. 375–389.

[7] Cundall, P. A., and Strack, O. D., 1979, "A Discrete Numerical Model for Granular Assemblies," Geotechnique, **29**(1), pp. 47–65.

[8] Campbell, C. S., 1990, "Rapid Granular Flows," Annu. Rev. Fluid Mech., **22**(1), pp. 57–90.

[9] Dunatunga, S., and Kamrin, K., 2015, "Continuum Modelling and Simulation of Granular Flows Through Their Many Phases," J. Fluid Mech., **779**(9), pp. 483–513.

[10] Jop, P., Forterre, Y., and Pouliquen, O., 2006, "A Constitutive Law for Dense Granular Flows," Nature, **441**(7094), pp. 727–730.

[11] Rojek, J., and Oñate, E., 2008, "Multiscale Analysis Using a Coupled Discrete/Finite Element Model," Interact. Multiscale Mech., **1**(1), pp. 1–31.

[12] Andrade, J., Avila, C., Hall, S., Lenoir, N., and Viggiani, G., 2011, "Multiscale Modeling and Characterization of Granular Matter: From Grain Kinematics to Continuum Mechanics," J. Mech. Phys. Solids, **59**(2), pp. 237–250.

[13] Guo, N., and Zhao, J., 2014, "A Coupled FEM/DEM Approach for Hierarchical Multiscale Modelling of Granular Media," Int. J. Numer. Methods Eng., **99**(11), pp. 789–818.

[14] Yamashita, H., Chen, G., Brauchler, A., Ruan, Y., Jayakumar, P., and Sugiyama, H., 2018, "Computer Implementation of Hierarchical FE-DE Multiscale Approach for Modeling Deformable Soil in Multibody Dynamics Simulation," ASME Paper No. DETC2018-86110.

[15] Henann, D. L., and Kamrin, K., 2014, "Continuum Thermomechanics of the Nonlocal Granular Rheology," Int. J. Numer. Methods Eng., **60**, pp. 145–162.

[16] Tasora, A., Serban, R., Mazhar, H., Pazouki, A., Melanz, D., Fleischmann, J., Taylor, M., Sugiyama, H., and Negrut, D., 2016, "Chrono: An Open Source Multi-Physics Dynamics Engine," *High Performance Computing in Science and Engineering* (Lecture Notes in Computer Science), T. Kozubek, ed., Springer, Berlin, pp. 19–49.

[17] Project Chrono, 2019, "Chrono: An Open Source Framework for the Physics-Based Simulation of Dynamic Systems," Project Chrono, University of Wisconsin-Madison, Madison, WI, accessed Mar. 7, 2019, https://projectchrono.org/

[18] Gurtin, M. E., Fried, E., and Anand, L., 2010, *The Mechanics and Thermodynamics of Continua*, Cambridge University Press, Cambridge, UK.

[19] Pritchard, P. J., and Mitchell, J. W., 2016, *Fox and McDonald's Introduction to Fluid Mechanics, Binder Ready Version*, Wiley, Hoboken, NJ.

[20] Ragui, K., Boutra, A., Bennacer, R., and Benkahla, Y. K., 2018, "Progress on Numerical Simulation of Yield Stress Fluid Flows (Part I): Correlating Thermosolutal Coefficients of Bingham Plastics Within a Porous Annulus of a Circular Shape," Int. J. Heat Mass Transfer, **126**, pp. 72–94.

[21] Wallevik, J. E., 2014, "Effect of the Hydrodynamic Pressure on Shaft Torque for a 4-Blades Vane Rheometer," Int. J. Heat Fluid Flow, **50**, pp. 95–102.
[22] Lagrée, P.-Y., Staron, L., and Popinet, S., 2011, "The Granular Column Collapse as a Continuum: Validity of a Two-Dimensional Navier–Stokes Model With a μ (i)-Rheology," J. Fluid Mech., **686**, pp. 378–408.
[23] Gray, J. P., Monaghan, J. J., and Swift, R., 2001, "SPH Elastic Dynamics," Comput. Methods Appl. Mech. Eng., **190**(49–50), pp. 6641–6662.
[24] Monaghan, J. J., 2000, "SPH Without a Tensile Instability," J. Comput. Phys., **159**(2), pp. 290–311.
[25] Monaghan, J. J., 2005, "Smoothed Particle Hydrodynamics," Rep. Prog. Phys., **68**(8), pp. 1703–1759.
[26] Chorin, A. J., 1968, "Numerical Solution of the Navier–Stokes Equations," Math. Comput., **22**(104), pp. 745–762.
[27] Liu, G., and Liu, M. B., 2003, *Smoothed Particle Hydrodynamics: A Meshfree Particle Method*, World Scientific Pub, Singapore.
[28] Adami, S., Hu, X., and Adams, N., 2012, "A Generalized Wall Boundary Condition for Smoothed Particle Hydrodynamics," J. Comput. Phys., **231**(21), pp. 7057–7075.
[29] Zhou, Y., Xu, B., Yu, A., and Zulli, P., 2002, "An Experimental and Numerical Study of the Angle of Repose of Coarse Spheres," Powder Technol., **125**(1), pp. 45–54.
[30] Oda, M., and Iwashita, K., 2000, "Study on Couple Stress and Shear Band Development in Granular Media Based on Numerical Simulation Analyses," Int. J. Eng. Sci., **38**(15), pp. 1713–1740.
[31] Ai, J., Chen, J.-F., Rotter, J. M., and Ooi, J. Y., 2011, "Assessment of Rolling Resistance Models in Discrete Element Simulations," Powder Technol., **206**(3), pp. 269–282.
[32] Geer, S., Bernhardt-Barry, M., Garboczi, E., Whiting, J., and Donmez, A., 2018, "A More Efficient Method for Calibrating Discrete Element Method Parameters for Simulations of Metallic Powder Used in Additive Manufacturing," Granular Matter, **20**(4), p. 77.
[33] Hairer, E., Norsett, S., and Wanner, G., 2009, *Solving Ordinary Differential Equations I: Nonstiff Problems*, Springer, Berlin.
[34] Chung, J., and Lee, J. M., 1994, "A New Family of Explicit Time Integration Methods for Linear and Non-Linear Structural Dynamics," Int. J. Numer. Methods Eng., **37**(23), pp. 3961–3976.
[35] Project Chrono Development Team. Chrono: An Open Source Framework for the Physics-Based Simulation of Dynamic Systems. Accessed: 2019-12-07.
[36] Kelly, C., Olsen, N., and Negrut, D., 2019, "Billion Degree-of-Freedom Granular Dynamics Simulation on Commodity Hardware," ASME Paper No. DETC2019-98055.
[37] Mazhar, H., Pazouki, A., Rakhsha, M., Jayakumar, P., and Negrut, D., 2018, "A Differential Variational Approach for Handling Fluid-Solid Interaction Problems Via Smoothed Particle Hydrodynamics," J. Comput. Phys., **371**, pp. 92–119.
[38] Rakhsha, M., Pazouki, A., Serban, R., and Negrut, D., 2019, "Using a Half-Implicit Integration Scheme for the SPH-Based Solution of Fluid-Solid Interaction Problems," Comput. Methods Appl. Mech. Eng., **345**, pp. 100–122.